ACS OMEGA

Open Access

http://pubs.acs.org/journal/acsodf

Article

Mineral Chemistry and Chronology Investigation of Uraninite in the Jinguanchong Uranium Deposit in Eastern Hunan Province and the Implications for Geological Significance

Pengfei Fan, Mangen Li,* Hongye Huang, Guangwen Huang, Yong Gu, Ke Wang, and Niannan Chen

Cite This: *ACS Omega* 2024, 9, 10782−10792

Read Online

ACCESS | Metrics & More | Article Recommendations

ABSTRACT: Jinguanchong deposit, a part of the Mingyuefeng ore field in eastern Hunan Province, China, is a typical perigranitic uranium deposit (a subtype of granite-related deposit) discovered recently with considerable uranium mineralization. Herein, uraninite, the primary ore mineral in the deposit, was investigated via scanning electron microscopy and electron probe microanalysis. Additionally, laser ablation−inductively coupled plasma−mass spectrometry was used for the first time to determine the in situ U−Pb age and the rare-earth element characteristics of uraninite. Uraninite mainly comprises UO_2, CaO, and PbO with a low ThO_2 content. Uraninite exhibits a low total content of rare-earth elements with a distinct fractionation between light and heavy rare-earth elements while displaying a negative Eu anomaly. The presence of major elements and rare-earth elements in uraninite suggests its formation within a hydrothermal environment at moderate to low temperatures below 350 °C, thereby classifying the Jinguanchong deposit as a typical hydrothermal vein-type uranium deposit. The uranium metallogenic age is determined to be 93.8 ± 1.4 Ma, falling within the midlate Cretaceous period. This age corresponds to the Mesozoic lithospheric extension and thinning events (approximately 85−95 Ma) in South China, suggesting that the formation of the Jinguanchong uranium deposit might be associated with the tectonic dynamics of lithospheric extension and thinning.

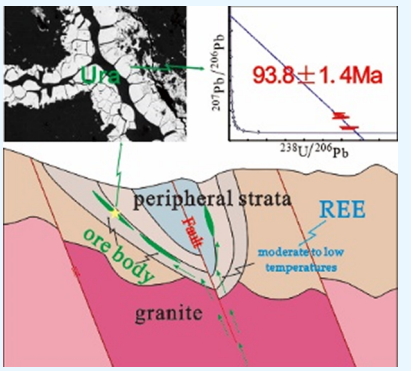

1. INTRODUCTION

Uraninite, a prevalent natural uranium oxide, is widely distributed in various hydrothermal and surficial uranium deposits. The age of its formation corresponds to the ore-forming age of deposits. Therefore, it is considered an ideal component for determining the metallogenic age of such deposits.[1−6] The rapid development of in situ microanalytical dating techniques in recent years has boosted the in situ U−Pb dating of uranium minerals. Luo et al. identified the ore-forming ages of the Xianshi uranium deposit via secondary ion mass spectrometry (SIMS)-based in situ U−Pb dating, yielding the ages of three mineralization stages as 135 ± 4, 113 ± 2, and 104 ± 2 Ma.[7] Bonnetti et al. further studied the ore-forming ages of the Baishuizhai uranium deposit (175 ± 16 Ma) via in situ U−Pb SIMS dating.[8] Wu et al. determined the formation age of the Guangshigou uranium deposit via laser ablation−inductively coupled plasma−mass spectrometry (LA−ICP−MS)-based in situ U−Pb dating as 405 ± 3.0 Ma.[9] Guo et al. determined the ore-forming age of the Zhangjia uranium deposit via LA−ICP−MS-based in situ U−Pb dating as 69.4 ± 4.9 Ma.[10] The in situ U−Pb dating technology has various advantages compared to the traditional uranium mineral dating method such as a high spatial resolution and minimal sample consumption. It can provide multiple age data of a mineral in the microscale range and effectively constrain and reflect the metallogenic age of uranium deposits.[11,12]

The Jinguanchong uranium deposit (JUD) is located within the boundaries of Xintai Village, Hejiaqiao Township, Liling City; Shuangfu Village, Daqiao Township, You County; and Hunan Province, China. It belongs to the Mingyuefeng ore field in the eastern Hunan Province. The recent increase in drilling activities in the Jinguanchong deposit led to the discovery of a high-grade ore body outside the Yajiangqiao rock pluton. The field geological investigation data of the past 2 years show that the majority of the ore body of the JUD exists within the peripheral strata surrounding the Yajiangqiao granitic pluton. Hence, JUD is considered a perigranitic uranium deposit (a subtype of granite-related deposit, while the other subtype is the endogranitic deposit), which is not a major industrially used uranium deposit in China but is more commonly found in European regions. The Pribram uranium deposit in the Czech Republic is a typical perigranitic uranium

Received: December 6, 2023
Revised: February 5, 2024
Accepted: February 9, 2024
Published: February 20, 2024

deposit with >68,000 t of U_3O_8.[13] The mineralized host rocks belong to Precambrian and Cambrian clastic rock formations, and their metallogenic age is ~270 Ma.[14−16] The Niederchlem−Alberode uranium deposit in Germany has a uranium resource of ~84,460 t. The ore veins are associated with the subtle thermal metamorphic aureole of the Erzgebirge granitic pluton outer contact zone, and the surrounding rocks comprise black shale and carbonaceous slate. The metallogenic age of this deposit is estimated to be between 318 and 325 Ma.[17] Similarly, the Ronneburg mining district (Germany) has yielded 216,000 tons of uranium and is one of the largest uranium mining sites worldwide. It has two metallogenic ages: 266 ± 42 and 110 ± 5 Ma.[14,18−21] These examples further highlight the significance of perigranitic uranium deposits in the field of uranium geology.

To the best of our knowledge, there have been no prior reports on the metallogenic age of the JUD and the in situ trace composition characteristics of uraninite. However, uranium metallogenic ages, chemical composition of uranium minerals, and other factors play an important role in understanding the geological condition, metallogenic mechanism, and comprehensive utilization of the deposit.[22−28] Therefore, a study on the mineralization characteristics and metallogenic ages of the high-grade ore bodies in the peripheral formation of the JUD is necessary. Herein, we focus on identifying the uranium ore present in the high-grade ore body of the JUD based on the field geological survey and rock and mineral identification. We studied the mineral chemistry and isotope geochronology to accurately determine the uranium mineralization characteristics and metallogenic age of the JUD via scanning electron microscopy (SEM)-based, electron probe microanalysis (EPMA)-based, and LA−ICP−MS-based in situ microarea analysis. The objective was to enhance the theoretical understanding of metallogenesis regarding this deposit, thereby providing a necessary foundation for exploration activities and efficient utilization.

2. GEOLOGICAL SETTING OF THE DEPOSIT

The tectonic suture zone between the Yangtze and Cathaysia blocks is a complex tectonic belt formed by multiple tectonic styles resulting from multiple episodes of orogenic events.[29−32] The JUD is located close to this tectonic suture zone (Figure 1a) and belongs to the western branch of the NNE-trending strike−slip orogenic belt within the eastern intracontinental domain of the South China block. The regional tectonic setting falls within an echelon strike−slip fault system situated between the Xiushui−Hengshan and Dongxing−Lingshan fault zones.[33]

The exposed stratigraphy in the study area from the oldest to the youngest consists of the Middle to Upper Proterozoic Lengjiaxi Group (Pt_2ln), Devonian Tiaomajian Formation (D_2t), Devonian Qiziqiao Formation (D_2q), Devonian Shetianqiao Formation (D_3s), Devonian Xikuangshan Formation (D_3x), Carboniferous Yanguan Stage (C_1y), and Quaternary Fourth Series (Q) (Figure 1b).[34] The Lengjiaxi Group represents the basement strata in the region comprising light gray, bluish gray, greenish phyllite, and schist with sandy slate. The Tiaomajian Formation primarily comprises yellowish-green metamorphic quartz sandstone and siltstone. The Qiziqiao Formation is mainly distributed in a narrow strip in the northeast of the Yajiangqiao rock pluton comprising carbonaceous argillaceous limestone and interbedded thin layers of mudstone and sandstone with locally observed

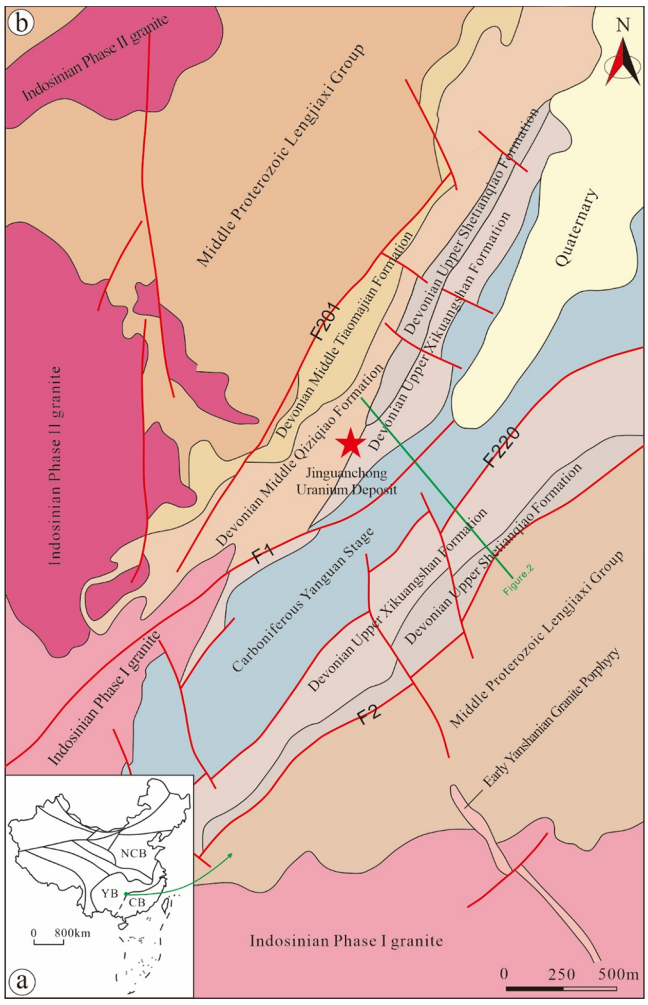

Figure 1. Schematic diagram of the tectonic location of the Jinguanchong uranium deposit (a) and its geological sketch (b).

yellowish-gray mudstone in the low regions. The Qiziqiao Formation serves as the main target layer for mineral exploration in the Mingyuefeng ore field and represents the primary host layer for the large ore bodies of the JUD. The Shetianqiao Formation exhibits lithology characterized by massive deposits of white and light brown crystalline dolomite and limestone. The upper regions of the Xikuangshan Formation comprise gray quartz sandstone, while the lower regions are dominated by gray−brown banded mudstone. The rock type of the Yanguan stage primarily includes carbonaceous argillaceous limestone and carbonaceous mudstone.[35,36] The predominant outcropping igneous rock in the study area is the Yajiangqiao rock pluton distributed in the northern segment of the Chuankou−Mingyuefeng uplift. It is characterized by an overall stock-like intrusion into the Lengjiaxi Group and Banxi Group, representing a multistage composite granite pluton. The diagenetic age can be categorized into two stages: 244−251 and 212−213Ma.[37] The main geological structures within the mining area include the Dazhang−Hejiaqiao inclined fault, two deep faults F1 and F2, and numerous interlayer and intralayer fracture zones. The structural trends of these features are generally oriented in the NE−NNE direction, accompanied by a minor occurrence of later NW-oriented faults, which tend to crosscut the NE-oriented structures.

https://doi.org/10.1021/acsomega.3c09746
ACS Omega 2024, 9, 10782−10792

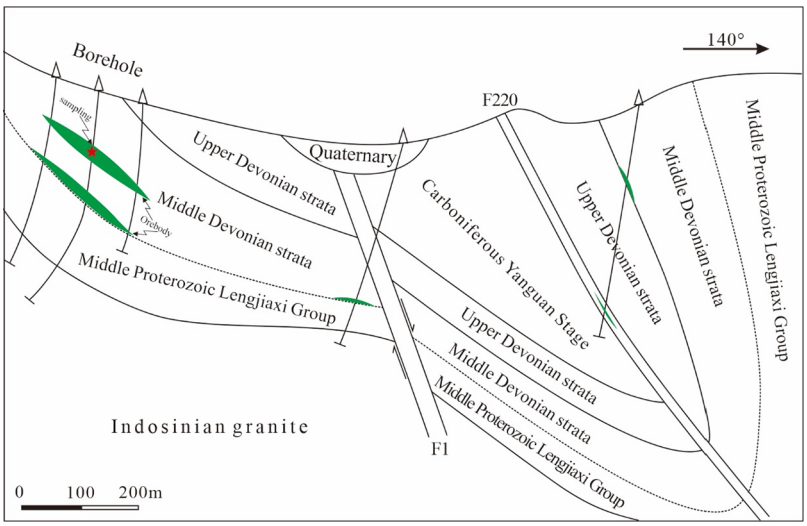

Figure 2. Geological profile sketch of the Jinguanchong uranium deposit.

The JUD is located at the northeastern outer contact zone of the Yajiangqiao rock granitic pluton and the southwestern terminus of the Dazhang−Hejiaqiao syncline. The primary orebody units are in contact with the granite pluton. The favorable strata for mineralization comprise Qiziqiao Formation (D_2q) and Lengjiaxi Group (Pt_2ln). Among these formations, carbonaceous argillaceous limestone in the Qiziqiao Formation represents the predominant type of enriched ore-bearing strata and lithology. The formation and distribution of valuable ore bodies are influenced by contacts between different layers and interlayer fracture zones. The interlayer fracture zones within the Qiziqiao Formation are a major structural factor for their formation. This deposit primarily yields uranium-rich ores characterized by high-grade pink calcite−uraninite minerals with considerable thickness (Figure 2).

3. SAMPLE COLLECTION AND ANALYTICAL METHODS

3.1. Sample Collection and Preparation. The uranium ore samples in this study were collected from large ore bodies in the periphery of the JUD. The ore rocks comprise black carbonaceous argillaceous limestone with evident rock fragmentation and developed fractures, which are filled with pink calcite (Figure 3a). Uranium minerals are primarily distributed within calcite veins. The corresponding thin and ore-polished sections of the samples were prepared at the Analysis and Testing Center of Changsha Uranium Geology Research Institute. Mineralogical identification was conducted using a polarizing microscope in the laboratory, initially identifying the minerals and areas of interest. Subsequently, the samples were analyzed via SEM and EPMA.

3.2. Analytical Methods. The samples were analyzed via SEM at the State Key Laboratory of Nuclear Resources and Environment at East China University of Technology using an FEI Nova Nano SEM450 instrument with resolutions of 1.0 nm (at 15 kV) and 1.4 nm (at 1 kV) in an acceleration voltage of 15 kV. SEM is equipped with an Oxford X-Max20 energy dispersive spectrometer capable of qualitative point analysis. SEM was primarily used for the examination of the uranium mineral morphology and identification of suitable microregions for in situ dating sites.

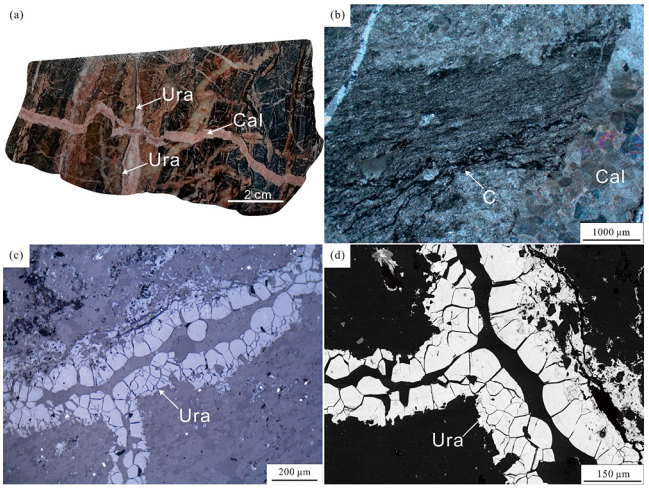

Figure 3. Uranium ore samples from the Jinguanchong deposit and microscope images. (a) Uranium ore sample, the black carbonaceous argillaceous limestone breccia is cemented by flesh-red calcite. (b) Transmitted polarized light image of carbonaceous argillaceous limestone. (c) Reflected polarized light photograph of uraninite. (d) Backscattered electron image of uraninite. Ura: uraninite, Cal: calcite, and C: carbonaceous.

EPMA was performed for quantitative composition analysis by Wuhan Microbeam Analysis Co., Ltd. using a Jeol-8230 instrument. The test was conducted with an acceleration voltage of 15 kV and an acceleration current of 20 nA with a beam spot diameter of 1 μm. The measurement time for the characteristic peaks of Si, Al, Na, K, Ca, Mg, Fe, Mn, P, U, Th, and Pb was 10 s and La, Ce, Yb, Y, and Ti was 20 s. The measurement time for the top and bottom background was half of the peak measurement time. The standard samples used for element testing were olivine (Si), corundum (Al), jadeite (Na), orthoclase (K), diopside (Ca and Mg), pyrope (Fe), rhodonite (Mn), rutile (Ti), apatite (P), thorium metal (Th), uraninite (U), galena (Pb), and rare-earth element (REE)-containing glass. Quantitative data were calibrated using the atomic number (Z), absorption (A), and secondary fluorescence (F) (ZAF) correction method. The detection limit for elements was 200×10^{-6} with 1.5% main element error and 5.0% trace

https://doi.org/10.1021/acsomega.3c09746
ACS Omega 2024, 9, 10782−10792

element error. EPMA was used for the analysis of the major chemical composition of uranium minerals.

The in situ U−Pb dating and in situ REE content of uraninite was detected at Wuhan Samplesution Analytical Technology Co., Ltd. via LA−ICP−MS analysis. The detailed operating process, data processing, and calibration strategies are the same as described by Zong et al.[38,39] The GeolasPro LA system comprises a COMPexPro 102 ArF 193 nm excimer laser and MicroLas optical system coupled with an Agilent 7900 ICP−MS. Helium was used as the carrier gas during LA, and argon was used as the auxiliary gas to adjust sensitivity. The two gases were mixed through a T-shaped connector before entering the ICP, and the LA system was equipped with a signal-smoothing device.[40] The laser spot size and frequency for the analysis were 16 μm and 1 Hz, respectively. Uraninite standard GBW04420 was used as an external standard for U−Pb isotope calibration. The trace REE compositions of uraninite were calibrated against NIST SRM 610. Each analysis incorporated a background acquisition of 20−30 s followed by 50 s data acquisition from the sample. An Excel-based software ICPMSDataCal was used to perform the off-line selection and integration of the background and analyzed signals, time-drift correction, and quantitative calibration for trace element analysis.[41,42] U−Pb age concordia diagrams and age-weighted average calculations were conducted using Isoplot/Ex_ver3.[43]

4. RESULTS

4.1. Petrographic Characteristics. The freshly exposed surface of the uranium ore is brown and black, accompanied by developed multiple pink calcite veins (Figure 3a). The microscopic observation of the thin sections of the ore sample reveals a predominant host rock of carbonaceous argillaceous limestone (Figure 3b) with a fine-grained and laminar structure. The ore contains abundant microcrystalline calcite, cryptocrystalline−micaceous clay minerals, mica, and opaque carbonaceous components. Microcrystalline calcite particles are flattened and elongated in a preferred orientation. Carbonaceous argillaceous limestone in the mineralized section is intensely fragmented, forming angular fragments, which are cemented by later-stage pink calcite. Uranium minerals are closely associated with pink calcite (Figure 3a,b) primarily comprising uraninite. The reflection of uraninite appears steel gray and occurs as spherical or grape-like aggregates, forming fine vein−like structures (Figure 3c). A few uraninite samples exhibit desiccation cracks. Uraninite aggregates are distributed along the edges of the carbonaceous argillaceous limestone fragments and extend to the interior area. Backscattered electron imaging shows that uraninite is uniformly bright white with some granular uraninite displaying concentric banding structures (Figure 3d), where the outer portion has slightly higher grayscale values than that of the inner portion. Uraninite might transform into fibrous secondary uranium minerals in some cases. A detailed observation via a polarizing microscope and scanning electron microscope infers that the rocks in the formation underwent cementation by late-stage calcite after fragmentation. Simultaneously, uraninite precipitated from hydrothermal solutions during the formation of calcite. Vein aggregate uraninite was formed around the breccias within the original rock formation, indicating that uranium mineralization did not occur during other stages.

4.2. Electron Probe Microanalysis (EPMA) of Uraninite. EPMA was performed on uraninite in the samples. Ten points were tested, and the analysis results are shown in Table 1. The main constituent elements of uraninite are U, Ca, and Pb with trace amounts of Na, P, Fe, Mn, Ce, Y, and other elements. The contents of different oxides and elements in uraninite are as mentioned here: (i) UO_2: 88.57−90.60% with an average of 89.95%, (ii) CaO: 5.21−6.58% with an average of 6.15%, (iii) calcium: a high content, (iv) PbO: 1.22−1.93% with an average 1.58%, (v) SiO_2: 0−0.45% with an average of 0.09%, (vi) NaO: 0−0.24% with an average of 0.09%, (vii) FeO: 0−0.67% with an average of 0.50%, and (viii) MnO: 0.25−0.32% with an average of 0.28%. K, Ti, and Th elements were not detected.

4.3. Microscale In Situ U−Pb Dating of Uraninite. LA−ICP−MS-based in situ U−Pb isotopic dating analysis was conducted on uraninite collected from the rich ore body of the JUD. The samples were analyzed via polarized light microscopy and SEM. The particles of uraninite free from cracks with flat crystal faces and displaying uniform reflective and backscattered electron image colors were chosen for the in situ microanalysis of U−Pb isotopes via LA−ICP−MS. Such minerals are commonly found in uranium ores and their formation age can represent the age of ore mineralization. The calibration of this test was conducted using the national-level standard material GBW04420. The isotope ratios were calibrated using the Chinese-certified reference material (GBW04420) as an external reference. The calibrated age of the standard sample is 69.8 ± 0.6 Ma.[38] A total of 15 valid data points are obtained from measurements, as shown in Table 2. Figure 4a shows the schematic diagram of the position of test points. The Tera−Wasserburg (T−W) concordia diagram was used for interpreting the results. The T−W diagram proposed by Tera and Wasserburg obviates the need for the common lead correction, which places $^{238}U/^{206}Pb$ and $^{207}Pb/^{206}Pb$ on the x- and y-axes to generate an incongruent line. The bottom intersection point of this incongruent line with the concordia line represents the age of sample formation, while the top intersection point represents the composition of common Pb isotopes.[44,45] The $^{206}Pb/^{238}U$ of young geological samples provides a more accurate indication of uraninite crystallization time. Nonradiogenic Pb isotopes are deduced based on geological expertise and measured data using the measured $^{207}Pb/^{206}Pb$ ratio, enabling the calculation of a weighted average age in this study. Both ages coincide, indicating that the JUD has a uranium metallogenic age of 93.8 ± 1.4 Ma (Figure 4). This age corresponds to the main ore-forming period of the JUD with the midlate Cretaceous period.

4.4. Microscale In Situ REE Analysis of Uraninite. The in situ REE concentrations in uraninite were simultaneously determined via U−Pb isotope analysis. The corresponding results are presented in Table 3. The ∑REE content of uraninite ranges from 110.21 × 10^{-6} to 292.55 × 10^{-6}, exhibiting a relatively low overall abundance with an average value of 193.42 × 10^{-6}. The LREE content ranges from 87.85 × 10^{-6} to 258.29 × 10^{-6} with an average value of 160.01 × 10^{-6}. The HREE content ranges from 14.46 × 10^{-6} to 43.69 × 10^{-6} with an average value of 33.41 × 10^{-6}. The LREE/HREE ratio ranges from 3.80 to 8.41, indicating a clear fractionation pattern between LREE and HREE. The $(La/Yb)_N$ value ranges from 4.72 to 21.12 with an average value of 7.84 (>1), indicating a significant enrichment of light REEs. The δCe values range from 0.92 to 1.05 with an average value of 1.00,

https://doi.org/10.1021/acsomega.3c09746
ACS Omega 2024, 9, 10782−10792

Table 1. EPMA Quantitative Point Analysis Data of Uraninite (%)[a]

no.	Y_2O_3	P_2O_5	FeO	K2O	CaO	TiO_2	Al_2O_3	SiO_2	La_2O_3	Ce_2O_3	PbO	MnO	ThO_2	UO_2	Yb_2O_3	Na_2O	MgO	Total
1	0.13	—	0.67	—	5.47	—	0.02	0.45	0.08	0.37	1.89	0.32	—	89.11	—	0.08	0.02	98.60
2	0.26	0.05	0.36	—	5.86	—	—	0.11	0.06	0.30	1.62	0.28	—	90.51	0.07	0.15	0.01	99.62
3	0.22	0.05	0.64	—	5.21	—	0.01	0.20	0.14	0.42	1.86	0.25	—	89.23	—	0.24	—	98.46
4	0.20	—	0.54	—	6.48	—	—	0.08	0.02	0.25	1.93	0.25	—	89.88	0.03	0.08	—	99.73
5	0.31	0.11	0.44	—	6.58	—	—	0.03	—	0.10	1.37	0.26	—	90.45	0.10	0.11	—	99.88
6	0.23	0.06	0.60	—	6.53	—	—	—	—	—	1.47	0.28	—	90.47	0.04	0.12	0.01	99.81
7	0.02	0.07	0.44	—	6.21	—	0.01	0.02	—	0.04	1.30	0.31	—	90.60	—	0.13	—	99.14
8	0.18	0.02	0.40	—	6.37	—	—	—	0.07	0.12	1.22	0.25	—	90.29	0.22	0.11	—	99.24
9	0.03	0.04	0.45	—	6.48	—	—	0.02	—	0.27	1.74	0.31	—	88.57	0.03	0.13	0.01	98.07
10	0.22	0.01	0.48	—	6.29	—	—	0.03	—	0.04	1.43	0.28	—	90.38	0.01	0.11	0.01	99.27

[a]Notes. The symbol"—"indicates values below the detection limit.

suggesting no Ce anomaly compared to other REEs. The δEu value ranges from 0.39 to 0.81 with a mean value of 0.60, indicating a clear negative anomaly.

5. DISCUSSION

5.1. Chemical Characteristics and Significance of Uraninite. The chemical composition of uraninite is influenced by physicochemical conditions during its formation, leading to element migration and substitution. Therefore, the actual chemical formula of uraninite is more complex than the ideal UO_2 stoichiometry.[46,47] Uraninite has elevated UO_2 (88.57−90.60%) and CaO (5.21−6.58%) contents in the uranium-rich ore body of the JUD, while the ThO_2 content is notably below the detection limit. The high CaO content in uraninite is attributed to the similar ionic radii of U^{4+} and Ca^{2+} (1.05 and 1.06 Å), allowing easy substitution of U^{4+} by Ca^{2+} in the lattice structure of uraninite.[48,49] Petrographic studies suggest that calcium is abundant in uranium conditions where U^{4+} can be replaced by Ca^{2+} with calcite being the main associated mineral. Uraninite undergoes U^{4+} and Th^{4+} substitution during hydrothermal crystallization because Th^{4+} (0.105 nm) and U^{4+} (0.1 nm) have similar ionic radii and geochemical properties. U has different solubilities under various oxidation states, and the oxidizing nature of low-temperature hydrothermal fluids facilitates U migration. Meanwhile, Th is relatively stable in a low- to moderate-temperature environment with low solubility in hydrothermal fluids. Thus, it is less susceptible to migration by oxidizing fluids. The solubility of Th is high in a high-temperature environment (>350 °C), making it more prone to enter into uranium oxide lattices. Hence, a low Th content is present in uranium oxides formed in an environment below 350 °C. The U/Th ratio of uranium minerals is an important indicator of the crystallization temperature of hydrothermal uranium deposits. A U/Th ratio <100 indicates a high crystallization temperature or formation under a magmatic environment, while a U/Th ratio >1000 suggests a low crystallization temperature.[50−52] The tested uraninite samples have a UO_2 content >80% in the present study, while ThO_2 is below the detection limit. This preliminary inference suggests that the U/Th ratio of uraninite might be >1000, indicating a formation temperature of <350 °C for the JUD.

REEs present in uraninite can be utilized for determining its formation environment and temperature. Uraninite formed in high-temperature magma or a metamorphic environment has a significantly high content of ∑REE (>1%). A substantial influx of REEs occurs within uraninite owing to the expansive nature of uraninite under these temperatures, resulting in an indistinct fractionation between LREEs and HREEs. This forms a relatively flat REE pattern. The ∑REE content of uraninite formed in hydrothermal environments at moderate to low temperatures (<350 °C) is low (<1%). REEs are influenced by the source and crystalline phase of uraninite, leading to fractionation among REEs and the potential formation of an Eu anomaly. The REE pattern exhibits a discernible slope, which provides an insight into the type of uranium mineralization to a certain extent.[51,53,54]

The REEs of uraninite samples in this test are present at a concentration of <1%. The LREE/HREE ratio and $(La/Yb)_N$ are significantly >1, indicating a pronounced fractionation between LREEs and HREEs. All sample points in this test are present within the low-temperature hydrothermal mineralization region in the (U/Th)−∑REE diagram (Figure 5a), while

https://doi.org/10.1021/acsomega.3c09746
ACS Omega 2024, 9, 10782−10792

Table 2. In Situ U−Pb Dating Results of Uraninite by LA-ICP-MS Micro-Area Analysis

number of test spot	$^{207}Pb/^{206}Pb$ ratio	$^{207}Pb/^{206}Pb$ 1sigma	$^{207}Pb/^{235}U$ ratio	$^{207}Pb/^{235}U$ 1sigma	$^{206}Pb/^{238}U$ ratio	$^{206}Pb/^{238}U$ 1sigma	$^{207}Pb/^{235}U$ age (Ma)	$^{207}Pb/^{235}U$ 1sigma	$^{206}Pb/^{238}U$ age (Ma)	$^{206}Pb/^{238}U$ 1sigma	Th $\times10^{-6}$	U $\times10^{-6}$
1	0.0853	0.0005	0.1849	0.0050	0.0156	0.0004	172	4.3	100	2.5	0.0144	754,219
2	0.0874	0.0005	0.1851	0.0038	0.0153	0.0003	172	3.3	98	1.9	0.0111	753,312
3	0.0889	0.0004	0.1897	0.0041	0.0154	0.0003	176	3.5	99	2.0	0.0210	753,244
4	0.0885	0.0004	0.1944	0.0044	0.0159	0.0003	180	3.8	102	2.2	0.0179	750,138
5	0.0854	0.0004	0.1889	0.0039	0.0160	0.0003	176	3.3	102	2.0	0.0080	750,289
6	0.0896	0.0004	0.1871	0.0029	0.0151	0.0002	174	2.5	97	1.5	0.0576	760,480
7	0.0873	0.0004	0.1818	0.0030	0.0151	0.0002	170	2.5	97	1.6	0.0184	755,756
8	0.0907	0.0005	0.2027	0.0036	0.0162	0.0003	187	3.0	104	1.8	0.0281	753,115
9	0.0872	0.0004	0.1848	0.0030	0.0154	0.0003	172	2.6	98	1.7	0.0577	756,503
10	0.0752	0.0004	0.1625	0.0031	0.0157	0.0003	153	2.8	100	2.0	0.0053	754,064
11	0.1810	0.0010	0.4278	0.0102	0.0170	0.0004	362	7.3	109	2.3	0.0363	768,401
12	0.1678	0.0018	0.3987	0.0106	0.0170	0.0003	341	7.7	109	2.0	0.3230	707,573
13	0.1542	0.0012	0.3562	0.0105	0.0166	0.0004	309	7.9	106	2.7	0.0596	735,669
14	0.1489	0.0006	0.3494	0.0076	0.0170	0.0004	304	5.8	109	2.5	0.0279	765,697
15	0.1570	0.0008	0.3549	0.0062	0.0164	0.0003	308	4.7	105	2.0	0.2283	740,727

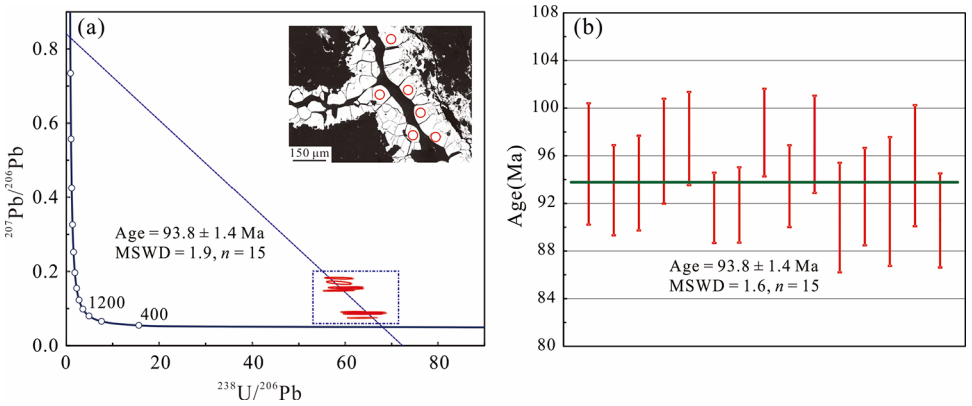

Figure 4. (a) Tera−Wasserburg concordia diagram and (b) weighted average age of the uraninite U−Pb age of the Jinguanchong deposit.

all sample points in this test are present within the moderate to low-temperature and high salinity hydrothermal fluid of the cogenetic crystallization phase in the $(LREE/HREE)_N-\sum REE$ diagram (Figure 5b). The REE pattern is compared to various types of uranium deposits around the world. The findings demonstrate that the hydrothermal vein-type uranium deposit congruently matches with the REE pattern (Figure 6). The δEu value is an indicator of the redox environment of the ore-forming fluid. Europium (Eu) is a variable valence element and predominantly exists as Eu^{3+} in the ore-forming fluid. However, a part of Eu^{3+} reduces to Eu^{2+} under a reducing condition, distinctly fractionating it from other REEs.[55] The test sample exhibits a pronounced negative Eu anomaly (δEu < 1), suggesting that uraninite in the JUD was formed in a reducing environment. Ce predominantly exists as Ce^{3+} with other REEs in the reducing ore-forming fluid, exhibiting negligible fractionation between them resulting in δCe ≈ 1. The presence of REEs in uraninite indicates that the JUD is a typical hydrothermal vein−type uranium deposit and uraninite precipitates from a low-temperature (<350 °C) hydrothermal fluid. The ore-forming fluid is characterized by high salinity and reducibility. The occurrence of the main ore bodies of the JUD within the peripheral contact zone of the Yajiangqiao rock pluton predicts that the ore should be guided by the metallogenic characteristics of carbonate−silicone−pelite type uranium deposits, which are commonly found in China. However, our study reveals that both major elements and REEs present in the uraninite of the JUD are from a moderate to low-temperature hydrothermal vein−type deposit. Therefore, it is crucial to primarily consider the metallogenic characteristics associated with hydrothermal vein−type uranium deposits during actual activities.

5.2. The Uranium Mineralization Tectonic Background. The South China composite continent, resulting from the multiple collisions between the Yangtze and Cathaysia island oceanic plates, is the fundamental basis for the NNE-oriented tectonic development along the border between Jiangxi and Hunan provinces. It establishes the primary structural pattern of the Mingyuefeng ore field.[56−58] The Pacific plate migrated northward since the Carnian period. Hence, the NNE-oriented boundary fault between Hunan and Jiangxi provinces underwent a transition from intracontinental subduction to intracontinental strike−slip motion. This transformation formed a series of large-scale NNE-oriented strike−slip faults along the border of Hunan and Jiangxi provinces in an approximately equidistant manner from north to south.[59] Notable examples are the Liling−Youxian and Chaling−Chenzhou faults. These fault structures control the tectonic development in the Mingyuefeng area while forming subsidiary faults within the Mingyuefeng ore field such as deep-seated faults (F1 and F2) in the JUD and secondary structures (F201 and F220) (Figure 1). The main deep faults of the JUD are F1 and F2, which are crucial ore-conducting structures. F201 and F220 play a significant role in controlling the

https://doi.org/10.1021/acsomega.3c09746
ACS Omega 2024, 9, 10782−10792

Table 3. In Situ REE Results of Uraninite by LA-ICP-MS Micro-Area Analysis ($\times 10^{-6}$)[a]

no.	La	Ce	Pr	Nd	Sm	Eu	Gd	Tb	Dy	Ho	Er	Tm	Yb	Lu
1	36.51	70.97	8.88	34.50	8.71	1.73	8.82	1.83	12.15	2.27	6.14	0.94	4.25	0.38
2	34.31	71.26	8.58	36.85	9.08	1.96	8.68	1.78	12.50	2.73	6.24	0.91	5.21	0.45
3	34.98	72.40	8.61	41.13	7.05	1.88	11.40	1.96	14.21	3.03	6.97	1.07	4.62	0.44
4	36.62	77.17	8.97	37.51	8.27	1.95	10.81	2.20	12.50	2.89	6.76	0.92	4.75	0.35
5	34.88	69.47	8.99	36.74	9.26	1.56	10.11	1.45	12.52	2.17	6.37	1.04	5.07	0.63
6	30.77	65.05	7.59	33.20	7.91	1.72	9.66	1.58	10.99	2.15	6.56	0.92	4.44	0.46
7	34.47	71.68	8.15	40.08	9.70	1.63	8.29	1.89	12.07	2.65	6.58	0.86	4.75	0.48
8	32.41	65.34	7.72	34.23	10.08	1.45	7.24	1.77	12.17	2.50	6.16	0.93	4.91	0.51
9	28.34	52.71	6.71	24.34	5.83	0.90	7.22	1.37	8.11	1.56	4.80	0.53	2.45	0.27
10	25.66	39.01	4.22	14.60	3.79	0.57	5.14	0.97	7.16	1.46	3.75	0.52	2.89	0.47
11	40.60	71.80	7.93	32.60	7.97	1.48	8.54	1.54	10.50	1.64	4.91	0.66	3.21	0.46
12	51.90	118.36	15.26	57.21	12.62	2.93	9.62	1.73	11.79	2.21	4.73	0.58	3.28	0.32
13	33.00	51.98	5.65	22.49	3.56	1.04	4.98	0.69	4.53	0.80	1.95	0.24	1.12	0.16
14	40.96	73.08	7.64	31.40	7.75	1.68	9.64	1.56	10.36	1.92	6.17	0.63	3.65	0.24
15	44.18	91.18	10.98	48.31	11.33	2.59	9.71	1.52	7.54	1.65	4.07	0.50	2.74	0.33

no.	$\sum$REE/$\times 10^{-6}$	LREE/$\times 10^{-6}$	HREE/$\times 10^{-6}$	LREE/HREE	$(La/Yb)_N$	δEu	δCe
1	198.07	161.30	36.77	4.39	6.16	0.60	0.97
2	200.55	162.04	38.50	4.21	4.72	0.67	1.02
3	209.74	166.05	43.69	3.80	5.44	0.64	1.02
4	211.68	170.48	41.20	4.14	5.53	0.63	1.04
5	200.28	160.91	39.37	4.09	4.93	0.49	0.96
6	183.01	146.25	36.76	3.98	4.97	0.60	1.04
7	203.28	165.72	37.56	4.41	5.21	0.56	1.05
8	187.43	151.24	36.19	4.18	4.74	0.52	1.01
9	145.15	118.83	26.32	4.52	8.31	0.42	0.94
10	110.21	87.85	22.36	3.93	6.38	0.39	0.92
11	193.89	162.42	31.48	5.16	9.07	0.55	0.98
12	292.55	258.29	34.26	7.54	11.34	0.81	1.03
13	132.19	117.73	14.46	8.14	21.12	0.75	0.93
14	196.68	162.52	34.17	4.76	8.05	0.59	1.01
15	236.63	208.58	28.06	7.43	11.58	0.76	1.02

[a]Notes. $\delta Eu = (Eu)_N/((Sm)_N \times (Gd)_N)^{1/2}$; $\delta Ce = (Ce)_N/((La)_N \times (Pr)_N)^{1/2}$.

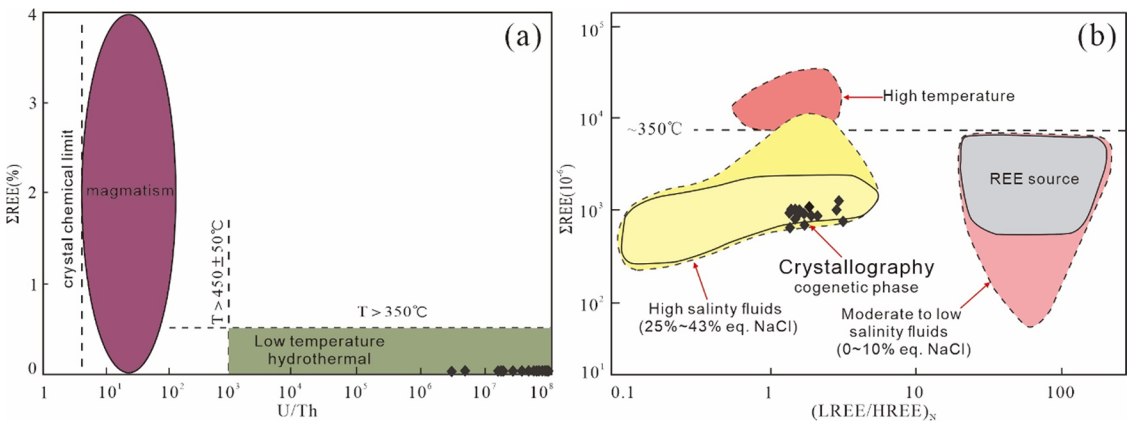

Figure 5. (a) (U/Th) vs $\sum$REE (modified from Frimmel et al.) and (b) $(LREE/HREE)_N$ vs $\sum$REE (modified from Mercadier et al.) diagrams of uraninite.

distribution of ore bodies. The faults cut through sedimentary or low-grade metamorphic rock sections. Particularly when the faults are nearly parallel to the fold structures, they tend to transform into interlayer fractured zones within fold bodies, such as the series of interlayer fractured zones found in the JUD.[60,61] The interlayer fracture zone comprises a significant ore-bearing structure within the deposit and serves as the primary distribution site for high-grade ore bodies.

The subduction rate of the Pacific plate beneath eastern China decreased since the early Cretaceous and the subduction shifted eastward. Thus, the entire South China inland region entered a regime of intracontinental extensional tectonics.[62,63] The strike−slip tectonic nature along the Hunan−Jiangxi province boundary began a transition from a convergent strike−slip mode to a divergent strike−slip mode. This tectonic transformation reached its climax during ∼100−90 Ma.[64] A significant number of strike−slip basins were also

https://doi.org/10.1021/acsomega.3c09746
ACS Omega 2024, 9, 10782−10792

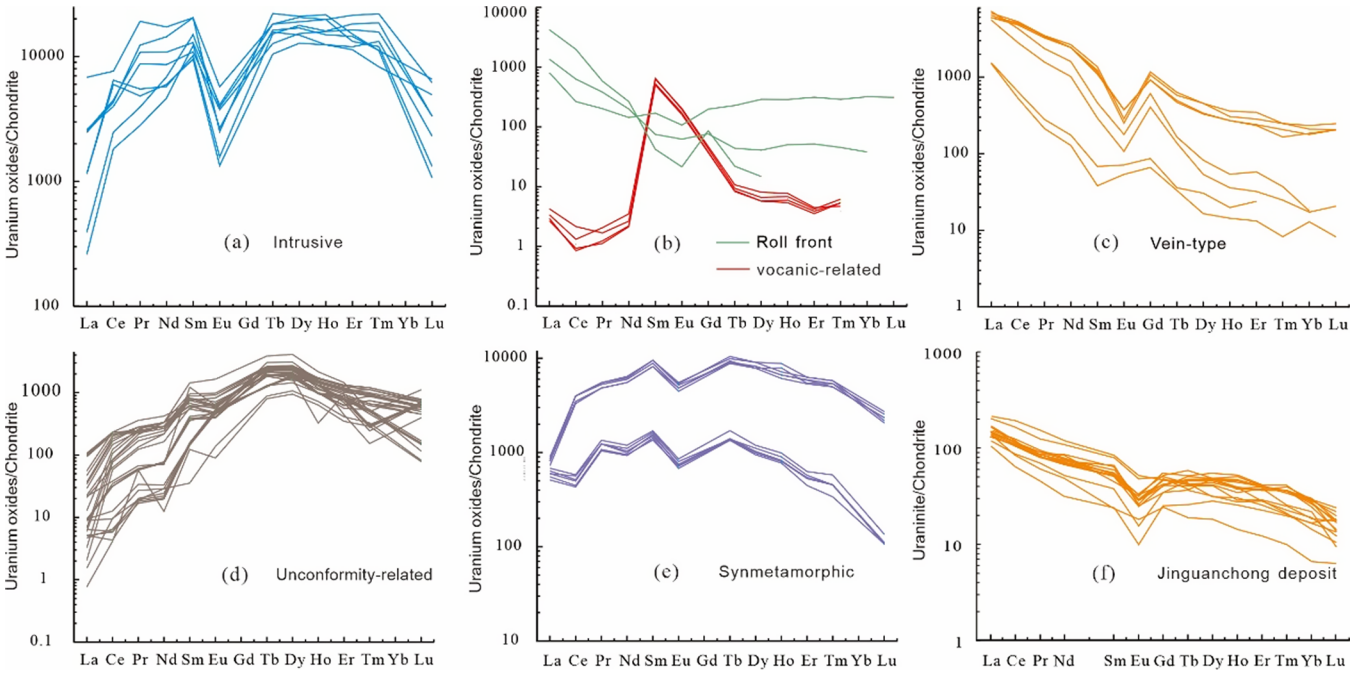

Figure 6. (a−e) Chondrite-normalized rare-earth element patterns of uranium oxides from six different types of uranium samples (modified following Mercadier et al.) and from the Jinguanchong deposit (f).

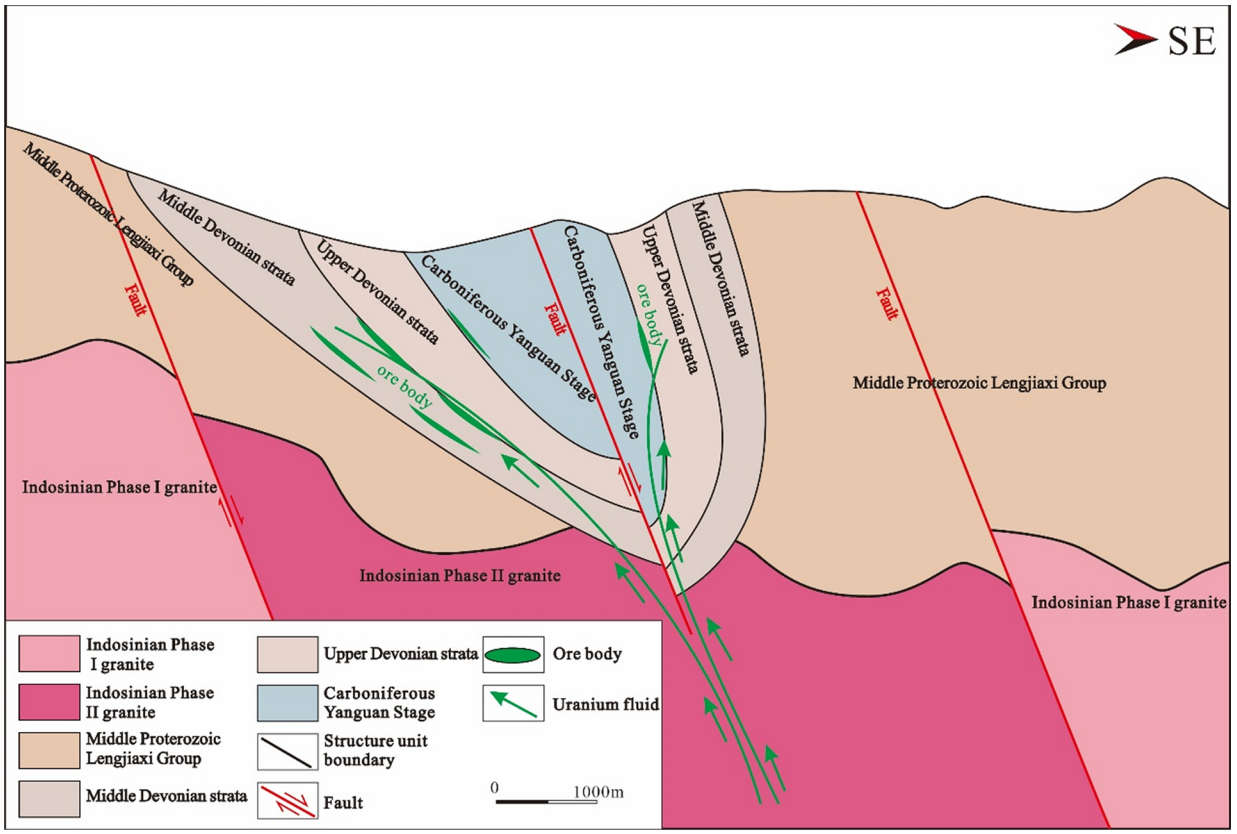

Figure 7. Metallogenic model diagram of the Jinguanchong deposit.

formed during this period, such as the Liyou Basin near the JUD.[65] The South China region has undergone lithospheric extension and thinning since the Mesozoic period, which mainly occurred in six stages: 145−135, 125−115, 110−100, 95−85, 75−70, and 55−45 Ma.[64,66,67] The formation age of the major ore body in the JUD coincides with one of the lithospheric extensional events (95−85 Ma). The lithospheric extension caused the NNE strike−slip faults in the JUD to undergo a structural transition from convergent strike−slip to divergent strike−slip phase. The fault opening increased during the divergent strike−slip phase connecting the surface and deep crust. This resulted in the formation of a well-developed

https://doi.org/10.1021/acsomega.3c09746
ACS Omega 2024, 9, 10782−10792

fluid circulation system with both deep and shallow fault systems contributing to the circulation (Figure 7). Petrological investigations have revealed that calcite coexists as a mineral with uraninite in the JUD, indicating the presence of a substantial concentration of CO_2 within hydrothermal fluids associated with uranium. The dominant mineralizing agent of the hydrothermal uranium deposit in South China is predominantly CO_2 with mantle-derived characteristics, which is uniformly controlled by crustal extension.[64,66,68] The regional NNE-oriented fault zones in this area facilitated the connection between the lithospheric mantle and surface, enabling the ascent of CO_2 through the fault, a mineralizing agent derived from mantle degassing. Fluids at the surface and deep circulating mineralizing CO_2 within the fracture system of the Yajiangqiao rock pluton and strata facilitated the activation and migration of uranium in the rock pluton and strata.[69] The reactivation of the early formed NNE-trending structures such as F1, F2, F201, and F220 facilitated the migration of ore-bearing hydrothermal fluids and provided deposition spaces. These structures are conduits for the transportation of ore-bearing hydrothermal fluids into interlayer fractured zones of the Qiziqiao Formation (Figure 7). The temperature of ore-bearing hydrothermal fluids gradually decreases during upward migration, resulting in the formation of low-temperature hydrothermal fluids. Uranium precipitates from these low-temperature hydrothermal fluids and accumulates as ore bodies in favorable areas such as interlayer fractured zones within the JUD.

6. CONCLUSIONS

(1) The major element and REE composition of uraninite in the JUD suggests that this deposit can be classified as a moderate to low-temperature hydrothermal vein-type uranium deposit.

(2) The LA−ICP−MS-based in situ U−Pb dating of uraninite indicated that the uranium metallogenic age in the JUD is 93.8 ± 1.4 Ma corresponding to the middle to late Cretaceous.

(3) The age of uranium mineralization in the JUD is consistent with the timing of regional NNE-oriented divergent strike−slip fault tectonic activity, suggesting that uranium mineralization occurred during the Mesozoic−Cenozoic lithospheric extension and thinning dynamics in South China.

AUTHOR INFORMATION

Corresponding Author

Mangen Li − *East China University of Technology, Nanchang 330006, China*; Email: mgli@ecut.edu.cn

Authors

Pengfei Fan − *East China University of Technology, Nanchang 330006, China; Changsha Uranium Geology Institute, Changsha 410007, China*; orcid.org/0009-0005-8528-9804

Hongye Huang − *Changsha Uranium Geology Institute, Changsha 410007, China*

Guangwen Huang − *School of Energency and Disaster Reduction, Qinghai Normal University, Xining 810008, China*

Yong Gu − *Changsha Uranium Geology Institute, Changsha 410007, China*

Ke Wang − *Changsha Uranium Geology Institute, Changsha 410007, China*

Niannan Chen − *East China University of Technology, Nanchang 330006, China*

Complete contact information is available at: https://pubs.acs.org/10.1021/acsomega.3c09746

Author Contributions

Writing-original draft, riting-editing, investigation, P.F.; conceptualization, M.L. and H.H.; visualization, K.W. and Y.G.; data curation, N.C.

Funding

This study was supported by the project "Uranium Geological Exploration in Mingmingfeng Area of Eastern Hunan" of Changsha Uranium Geology Institute. The authors would also like to acknowledge the financial support of East China University of Technology.

Notes

The authors declare no competing financial interest.

ACKNOWLEDGMENTS

The authors would like to thank Dr. Zhibo Zhang from China University of Mining and Technology for his guidance on the technical methods of this paper. The authors thank the "Mingyuefeng Project Team" of Changsha Uranium Geology Institute for their support of the field geological survey. The author especially thanks the reviewers for their reasonable comments on this paper.

REFERENCES

(1) Leroy, J. The margnac and fanay uranium deposits of the La Crouzille district (Western Massif Central, France); Geologic and fluid inclusion studies. *Econ. Geol.* **1978**, *73*, 1611−1634.

(2) Chipley, D.; Polito, P. A.; Kyser, T. K. Measurement of U-Pb Ages of uraninite and davidite by laser ablation-HR-ICP-MS. *Am. Mineral.* **2007**, *92*, 1925−1935.

(3) Cuney, M. The extreme iversity of uranium deposits. *Miner Deposita.* **2009**, *44*, 3−9.

(4) Zhang, L.; Wang, F.; Zhou, T.; Chen, Z. Contrasting U-Pb Geochronology and Geochemistry of Uraninite from the Xianshi and Xiwang Uranium Deposits, South China: Implications for Ore Genesis. *Ore Geol. Rev.* **2022**, *149*, No. 105120.

(5) Ballouard, C.; Poujol, M.; Mercadier, J.; Deloule, E.; Boulvais, P.; Baele, J. M.; Cuney, M.; Cathelineau, M. Uranium metallogenesis of the peraluminous leucogranite from the pontivy-rostrenen magmatic complex (French Armorican Variscan Belt): The result of long term oxidized hydrothermal alteration during strike-slip deformation. *Miner Deposita.* **2018**, *53*, 601−628.

(6) Huang, G.; Pan, C.; Pan, J.; Zhong, F.; Yan, J.; Xia, F.; Du, H.; Tao, Z.; Wan, J.; Kang, Q. The Geochronology Research on Uraninite in the Dashigou Carbonate-Type Molybdenum Deposit of East Qinling Area and Its Geological Significance. *Acta Geol. Sin.* **2023**, *97*, 1917−1937.

(7) Luo, J.; Hu, R.; Fayek, M.; Li, C.; Bi, X.; Abdu, Y.; Chen, Y. In-Situ Sims Uraninite U−Pb Dating and Genesis of the Xianshi Granite-Hosted Uranium Deposit. *South China. Ore Geol. Rev.* **2015**, *65*, 968−978.

(8) Bonnetti, C.; Liu, X.; Mercadier, J.; Cuney, M.; Deloule, E.; Villeneuve, J.; Liu, W. The Genesis of Granite-Related Hydrothermal Uranium Deposits in the Xiazhuang and Zhuguang Ore Fields, North Guangdong Province, SE China: Insights from Mineralogical, Trace Elements and U-Pb Isotopes Signatures of the U Mineralisation. *Ore Geol. Rev.* **2018**, *92*, 588−612.

(9) Wu, Y.; Qin, M.; Guo, D.; Fan, G.; Liu, Z.; Guo, G. The Latest in-Situ Uraninite U-Pb Age of the Guangshigou Uranium Deposit,

https://doi.org/10.1021/acsomega.3c09746
ACS Omega 2024, 9, 10782−10792

Northern Qinling Orogen, China: Constraint on the Metallogenic Mechanism. *Acta Geol. Sin.* **2018**, *92*, 2445−2447.
(10) Guo, C.; Qin, M.; Xu, H.; Ren, Z.; Zou, M.; Bai, Y.; Zhao, Y. Metallogenic Age of Zhangjia uranium deposit in Miaoershan uranium ore field, Guangxi: in-situ determination of uraninite microzone. *Earth Science.* **2020**, *45*, 72−89. in Chinese with English abstract.
(11) Cheng, L.; Zhang, C.; Song, H.; Cheng, Q. In-situ La-Icp-Ms Uraninite U-Pb Dating and Genesis of the Datian Migmatite-Hosted Uranium Deposit, South China. *Minerals* **2021**, *11*, 1098.
(12) Guo, G.; Bonnetti, C.; Zhang, Z.; Li, G.; Yan, Z.; Wu, J.; Wu, Y.; Liu, X.; Wu, B. SIMS U-Pb Dating of Uraninite from the Guangshigou Uranium Deposit: Constraints on the Paleozoic Pegmatite-Type Uranium Mineralization in North Qinling Orogen, China. *Minerals* **2021**, *11*, 402.
(13) Kribek, B.; Zak, K.; Spangenberg, J. E.; Jehlicka, J.; Prokes, S.; Kominek, J. Bitumens in the late variscan hydrothermal vein-type uranium deposit of Pribram, Czech Republic; Sources, radiation-induced alteration, and relation to mineralization. *Econ. Geol.* **1999**, *94*, 1093−1114.
(14) Bolonin, A. V.; Gradovsky, I. F. Supergene processes and uranium ore formation in the Ronneburg Ore Field. *Germany. Geol. Ore Deps.* **2012**, *54*, 122−131.
(15) Škácha, P.; Sejkora, J.; Plášil, J. Selenide mineralization in the příbram uranium and base-metal district (Czech Republic). *Minerals.* **2017**, *7*, 91.
(16) René, M.; Dolníček, Z.; Sejkora, J.; Škácha, P.; Šrein, V. Uraninite, Coffinite and Ningyoite from Vein-Type Uranium Deposits of the Bohemian Massif (Central European Variscan Belt). *Minerals.* **2019**, *9*, 123.
(17) IAEA. *Geological classification of uranium deposits and description of selected examples*; Vienna, 2018; pp 68−95.
(18) Lange, G., Freyhoff, G. Geology and mining in the uranium deposit of Ronneburg/Thuringia. In *Geologie und bergbau in der Uranlagerstaette Ronneburg/Thueringen*; Germany, 1991; pp 264−269.
(19) Vinokurov, S. F.; Rybalov, B. L.; Timofeev, A. V. *Uranium deposits of the ronneburg ore field (Germany): Tectonic setting, localization conditions and genetic Issues*; Czech Geological Survey: Czech Republic, 2002; pp 125−126.
(20) Geletneky, J.; Merten, D.; Büchel, G. *Prospects of Rare Earth Elements and Other Heavy Metals as Tracers in Acid Rock Drainage (Ard) at the Former Uranium Mining Site of Ronneburg*; Thuringia, 2003.
(21) Kampf, A.; Plasil, J.; Škoda, R.; Čejka, J. Michalskiite $Cu^{2+}Mg_3Fe^{3+}_{3.33}(VO_4)_6$, an Mg Analogue of Lyonsite, from the Ronneburg Uranium Deposit, Thuringia, Germany. *J. Geo-Sci.* **2022**, *67*, 33−40.
(22) Bowell, R. J.; Grogan, J.; Hutton, A. M.; Brough, C.; Penman, K.; Sapsford, D. J. Geometallurgy of Uranium Deposits. *Min. Eng.* **2011**, *24*, 1305−1313.
(23) Cuney, M.; Emetz, A.; Mercadier, J.; Mykchaylov, V.; Shunko, V.; Yuslenko, A. Uranium Deposits Associated with Na-Metasomatism from Central Ukraine: A Review of Some of the Major Deposits and Genetic Constraints. *Ore Geol. Rev.* **2012**, *44*, 82−106.
(24) Bruneton, P.; Cuney, M. *Uranium for Nuclear Power*; Hore-Lacy, I. Ed.; Woodhead Publishing, 2016; pp 11−52.
(25) Chi, G.; Haid, T.; Quirt, D.; Fayek, M.; Blamey, N.; Chu, H. Petrography, Fluid Inclusion Analysis, and Geochronology of the End Uranium Deposit, Kiggavik, Nunavut Canada. *Mineralium Deposita.* **2017**, *52*, 211−232.
(26) Wu, Y.; Ming, Q.; Guo, D.; Guang, F.; Zhang, Y. L.; Guo, G. Objective Constraint on the Metallogenic Mechanism. *Acta Geol. Sin.* **2018**, *92*, 2445−2447.
(27) Romer, R. L.; Cuney, M. Phanerozoic Uranium Mineralization in Variscan Europe − More Than 400 Ma of Tectonic, Supergene, and Climate-Controlled Uranium Redistribution. *Ore Geol. Rev.* **2018**, *102*, 474−504.
(28) Xia, Y.; Mou, C.; Wu, H. Uranium Occurrence State and Its Implication for Sandstone-Type Uranium Mineralization within the Hanbazhai Area of the Longchuanjiang Basin, China. *Minerals* **2023**, *13*, 1037.
(29) He, C.; Dong, S.; Santosh, M.; Chen, X. Seismic Evidence for a Geosuture between the Yangtze and Cathaysia Blocks, South China. *Sci. Rep.* **2013**, *3*, 2200−2207.
(30) Zhang, L. J. Lower Devonian Tempestites in Western Yangtze, South China: Insight from Zoophycos Ichnofabrics. *Geological Journal.* **2014**, *49*, 177−187.
(31) Madayipu, N.; Li, H.; Algeo, T. J.; Elatikpo, S. M.; Zheng, H.; Wu, Q. H.; Chen, Y. L.; Sun, W. B. Chemical and Boron Isotopic Compositions of Tourmalines from the Lianyunshan Nb-Ta Pegmatite in Northeastern Hunan, China: Insights into Fluid and Metallogenic Sources. *Ore Geol. Rev.* **2023**, *152*, No. 105263.
(32) Madayipu, N.; Li, H.; Ghaderi, M.; Soh, T. L.; Zhou, H. X.; Wu, Q. H.; Zheng, H.; Chen, Y. L.; Kang, F. Contrasting Nb-Ta Mineralization between the Mufushan and Lianyunshan Granites, South China: Evidence from Whole-Rock and Zircon Geochemistry and Geochronology. *Ore Geol. Rev.* **2023**, *158*, No. 105487.
(33) Li, J.; Li, Z.; Fu, Z. Analysis of ore-controlling structures in the Jinguanchong uranium deposit in Eastern Hunan. *Geol. Miner. Res. South China.* **1997**, 70−75. in Chinese with English abstract
(34) Jia, B. H. *Regional geology of Hunan province*; Hunan Provincial Geological Survey Institute: People's Republic of China, 2021; pp in Chinese with English abstract.
(35) Xie, Y. J. Comprehensive prospecting method model for the Jinguanchong uranium deposit. *World Nuclear Geosci.* **2006**, *1*, 38−43. in Chinese with English abstract
(36) Madayipu, N.; Li, H.; Algeo, T. J.; Elatikpo, S. M.; Heritier, R. N.; Zhou, H. X.; Zheng, H.; Wu, Q. H. Long-Lived Nb-Ta Mineralization in Mufushan, Ne Hunan, South China: Geological, Geochemical, and Geochronological Constraints. *Geosci. Front.* **2023**, *14*, No. 101491.
(37) Yu, Y.; Dai, P.; Zhou, Y.; Xie, F. Petrogenesis and Geodynamic Implications of the Late Triassic Bojites in Yajiangqiao Area, Hunan Province, South China. *Island Arc* **2020**, *29*, No. e12370.
(38) Zong, K.; Chen, J.; Hu, Z.; Liu, Y.; Li, M.; Fan, H.; Meng, Y. In-situ U-Pb dating of uraninite by FS-LA-ICP-MS. *Sci.China Earth Sci.* **2015**, *58*, 1731−1740.
(39) Zong, K.; Klemd, R.; Yuan, Y.; He, Z.; Guo, J.; Shi, X.; Liu, Y.; Hu, Z.; Zhang, Z. The Assembly of Rodinia: The Correlation of Early Neoproterozoic (Ca. 900ma) High-Grade Metamorphism and Continental Arc Formation in the Southern Beishan Orogen, Southern Central Asian Orogenic Belt (Caob). *Precambrian Research.* **2017**, *290*, 32−48.
(40) Hu, Z.; Zhang, W.; Liu, Y.; Gao, S.; Li, M.; Zong, K.; Chen, H.; Hu, S. Wave" signal-smoothing and mercury-removing device for laser ablation quadrupole and multiple collector ICP-MS analysis: Application to lead isotope analysis. *Anal. Chem.* **2015**, *87*, 1152−1157.
(41) Liu, Y.; Hu, Z.; Gao, S.; Günther, D.; Xu, J.; Gao, C.; Chen, H. In-situ analysis of major and trace elements of anhydrous minerals by LA-ICP-MS without applying an internal standard. *Chem. Geol.* **2008**, *257*, 34−43.
(42) Liu, Y.; Gao, S.; Hu, Z.; Gao, C.; Zong, K.; Wang, D. Continental and oceanic crust recycling-induced melt−peridotite interactions in the Trans-North China Orogen: U-Pb dating, Hf isotopes and trace elements in zircons from mantle xenoliths. *J. Petrol.* **2010**, *51*, 537−571.
(43) Ludwig, K. R. *ISOPLOT 3.00: A geochronological toolkit for microsoft Excel*; Berkeley Geochronology Center: California, Berkeley, 2003; p 39.
(44) Tera, F.; Wasserburg, G. J. U-Th-Pb Systematics in Three Apollo 14 Basalts and the Problem of Initial Pb in Lunar Rocks. *Earth and Planetary Science Letters.* **1972**, *14*, 281−304.
(45) Tera, F.; Wasserburg, G. J. U-Th-Pb Systematics in Lunar Highland Samples from the Luna 20 and Apollo 16 Missions. *Earth and Planetary Science Letters.* **1972**, *17*, 36−51.
(46) Kotzer, T. G.; Kyser, T. K. Petrogenesis of the proterozoic Athabasca Basin, Northern Saskatchewan, Canada, and its relation to

https://doi.org/10.1021/acsomega.3c09746
ACS Omega 2024, 9, 10782−10792

diagenesis, hydrothermal uranium mineralization and paleohydrogeology. *Chem. Geol.* **1995**, *120*, 45−89.
(47) Alexandre, P.; Kyser, K.; Layton, M. D.; Joy, B.; Uvarova, Y. Chemical Compositions of natural uraninite. *Canadian Miner.* **2015**, *53*, 595−622.
(48) Luo, J. C.; Hu, R. Z.; Fayek, M.; Bi, X. W.; Shi, S. H.; Chen, Y. W. Newly discovered uranium mineralization at ∼2.0 Ma in the Menggongjie granite-hosted uranium deposit, South China. *J. Asian Earth Sci.* **2017**, *137*, 241−249.
(49) Alexandre, P.; Kyser, T. K. Effects of cationic substitutions and alteration in uraninite, and implications for the dating of uranium deposits. *Canadian Miner.* **2005**, *43* (3), 1005−1017.
(50) Grandstaff, D. A Kinetic Study of the Dissolution of Uraninite. *Econ.Geol.* **1976**, *71*, 1493−1506.
(51) Frimmel, H.; Schedel, S.; Brätz, H. Uraninite chemistry as forensic tool for provenance analysis. *Appl. Geochem.* **2014**, *48*, 104−121, DOI: 10.1016/j.apgeochem.2014.07.013.
(52) Mukhopadhyay, J.; Mishra, B.; Chakrabarti, K.; De, S.; Ghosh, G. Uraniferous paleoplacers of the mesoarchean mahagiri quartzite, singhbhum craton, India: depositional controls, nature and source of > 3.0ga detrital uraninites. *Ore Geol. Rev.* **2016**, *72*, 1290−1306.
(53) Fryer, B. J.; Taylor, R. P. Rare Earth Element Distributions in Uraninites: Implications for Ore Genesis. *Chem. Geol.* **1987**, *63*, 101−108.
(54) Mercadier, J.; Cuney, M.; Lach, P.; Boiron, M. C.; Bonhoure, J.; Richard, A.; Leisen, M.; Kister, P. Origin of Uranium Deposits Revealed by Their Rare Earth Element Signature. *Terra Nova.* **2011**, *23*, 264−269.
(55) Brugger, J. I.; Etschmann, B.; Chu, Y. S.; Harland, C.; Vogt, S.; Ryan, C.; Jones, H. The Oxidation State of Europium in Hydrothermal Scheelite: In Situ Measurement by Xanes Spectroscopy. *Canadian Mineralogist.* **2006**, *44*, 1079−1087.
(56) Fu, Z.; Li, Z.; Zheng, D. Structural Development Pattern of NNE Strike-Slip Orogenic Belt in Hunan-Jiangxi Border Area. *Earth Sci. Front.* **1999**, 263−272. in Chinese with English abstract
(57) Huang, L.; Liu, C. Y.; Kusky, T. M. Cenozoic Evolution of the Tan−Lu Fault Zone (East China)—Constraints from Seismic Data. *Gondwana Research.* **2015**, *28*, 1079−1095.
(58) Madayipu, N.; Li, H.; Elatikpo, S. M.; Förster, M. W.; Zhou, H. X.; Zheng, H.; Wu, Q. H. Magmatic-Hydrothermal Evolution of Long-Lived Nb-Ta-(Sn) Mineralization in Lianyunshan, NE Hunan, South China. *GSA Bull.* **2023**, *135*, 2691−2709.
(59) Li, H.; Cao, J.; Algeo, T. J.; Jiang, W.; Liu, B.; Wu, Q. Zircons Reveal Multi-Stage Genesis of the Xiangdong (Dengfuxian) Tungsten Deposit South China. *Ore Geol. Rev.* **2019**, *111*, No. 102979.
(60) Bai, D. Y.; Huang, J. Z.; Liu, Y. R.; Wu, G. Y.; Ma, T. Q.; Wang, X. H. Determination of the Geological Structure Development Framework of the Mesozoic in Southeastern Hunan and the Hunan-Guangdong-Jiangxi Border Area. *China Geol.* **2005**, 33−46. in Chinese with English abstract
(61) Wu, L.; Mei, L.; Paton, D. A.; Liu, Y.; Guo, P.; Shen, C.; Liu, Z.; Luo, J.; Min, C.; Li, M. Late Cretaceous-Cenozoic Intraplate Extension and Tectonic Transitions in Eastern China: Implications for Intraplate Geodynamic Origin. *Mar. Petrol. Geol.* **2020**, *117*, No. 104379.
(62) Mao, J.; Pirajno, F.; Cook, N. Mesozoic Metallogeny in East China and Corresponding Geodynamic Settings an Introduction to the Special Issue. *Ore Geol. Rev.* **2011**, *43*, 1−7.
(63) Shu, L.; Deng, P.; Wang, B.; Tan, Z.; Yu, X.; Sun, Y. Lithology, Kinematics and Geochronology Related to Late Mesozoic Basin-Mountain Evolution in the Nanxiong-Zhuguang Area, South China. *Science in China Series D: Earth Sciences.* **2004**, *47*, 673−688.
(64) Hu, R.; Bi, X.; Zhou, M.; Peng, J.; Wen, C. S.; Liu, S.; Qi, H. Uranium Metallogenesis in South China and Its Relationship to Crustal Extension During the Cretaceous to Tertiary. *Econ. Geol.* **2008**, *103*, 583−598.
(65) Li, J.; Zhou, M.; Li, X.; Fu, Z.; Li, Z. The Hunan-Jiangxi Strike-Slip Fault System in Southern China: Southern Termination of the Tan-Lu Fault. *Journal of Geodynamics.* **2001**, *32*, 333−354.
(66) Hu, R.; Burnard, P.; Bi, X.; Zhou, M.; Peng, J.; Su, W.; Zhao, J. Mantle-Derived Gaseous Components in Ore-Forming Fluids of the Xiangshan Uranium Deposit, Jiangxi Province, China: Evidence from He. *Ar and C Isotopes. Chemical Geology.* **2009**, *266*, 86−95.
(67) Min, M. Z.; Luo, X. Z.; Du, G. S.; He, B. A.; Campbell, A. R. Mineralogical and Geochemical Constraints on the Genesis of the Granite-Hosted Huangao Uranium Deposit. *Se China. Ore Geol. Rev.* **1999**, *14*, 105−127.
(68) Hu, R.-H.; Li, C. Y.; Ni, S. J.; Liu, J.; Yu, J. S. Research on ΣCO_2 Source in Ore-Forming Hydrothermal Solution of Granite-Type Uranium Deposit South China. *Sci. China Chem.* **1993**, *36*, 1252−1262.
(69) Li, Z.; Fu, Z.; Li, J. NNE Strike-Slip Fault-Fluids-Uranium Metallogenic Dynamics Analysis in the Hunan-Jiangxi Border Area. *Mod. Geol.* **1998**, 67−76. in Chinese with English abstract

https://doi.org/10.1021/acsomega.3c09746
ACS Omega 2024, 9, 10782−10792